INTERNATIONAL JOURNAL FOR NUMERICAL METHODS IN FLUIDS
Int. J. Numer. Meth. Fluids 2005; **49**:521–547
Published online 24 June 2005 in Wiley InterScience (www.interscience.wiley.com). DOI: 10.1002/fld.1006

A level set characteristic Galerkin finite element method for free surface flows

Ching-Long Lin[1,*,†], Haegyun Lee[2,‡], Taehun Lee[1,§] and Larry J. Weber[2,¶]

[1]*Department of Mechanical and Industrial Engineering, IIHR—Hydroscience and Engineering, The University of Iowa, Iowa City, IA 52242-1527, U.S.A.*
[2]*Department of Civil and Environmental Engineering, IIHR—Hydroscience and Engineering, The University of Iowa, Iowa City, IA 52242-1527, U.S.A.*

SUMMARY

This paper presents a numerical method for free surface flows that couples the incompressible Navier–Stokes equations with the level set method in the finite element framework. The implicit characteristic-Galerkin approximation together with the fractional four-step algorithm is employed to discretize the governing equations. The schemes for solving the level set evolution and reinitialization equations are verified with several benchmark cases, including stationary circle, rotation of a slotted disk and stretching of a circular fluid element. The results are compared with those calculated from the level set finite volume method of Yue *et al.* (*Int. J. Numer. Methods Fluids* 2003; **42**:853–884), which employed the third-order essentially non-oscillatory (ENO) schemes for advection of the level set function in a generalized curvilinear coordinate system. The comparison indicates that the characteristic Galerkin approximation of the level set equations yields more accurate solutions. The second-order accuracy of the Navier–Stokes solver is confirmed by simulation of decay vortex. The coupled system of the Navier–Stokes and level set equations then is validated by solitary wave and broken dam problems. The simulation results are in excellent agreement with experimental data. Copyright © 2005 John Wiley & Sons, Ltd.

KEY WORDS: characteristic Galerkin method; unstructured mesh; free surface flow; level set method; solitary wave; broken dam

*Correspondence to: Ching-Long Lin, Department of Mechanical and Industrial Engineering, IIHR—Hydroscience and Engineering, The University of Iowa, Iowa City, IA 52242-1527, U.S.A.
†E-mail: ching-long-lin@uiowa.edu
‡E-mail: haelee@engineering.uiowa.edu
§E-mail: tlee@engineering.uiowa.edu
¶E-mail: larry-weber@uiowa.edu

Contract/grant sponsor: ONR; contract/grant number: N00014-01-1-0262
Contract/grant sponsor: Grant County, Washington

Received 29 September 2004
Revised 25 April 2005
Accepted 27 April 2005

1. INTRODUCTION

Modelling unsteady free surface flows has been a challenging task because of the moving interface which is known only at the initial time and has to be determined as part of the solution. A variety of numerical methods have been developed for free surface problems based upon either the moving-grid method or the fixed-grid method. The moving-grid method belongs to a Lagrange-type method which treats the free surface as the boundary of a moving surface-fitted grid. This method applies to either structured or unstructured grids, including strictly Lagrangian method, free Lagrangian method, and mixed Lagrangian–Eulerian method, among others [1]. In the moving-grid approach the free surface remains sharp and is computed precisely. The strictly Lagrangian method is restricted to the well-defined simple surface topology and small surface steepness, such as small amplitude water waves and slightly deformed air bubbles. To mitigate the difficulties in grid distortion, the free Lagrangian method [2] allows grids to switch their neighbours and reconnect with them. This method has been applied in droplet oscillation and droplet breakup in a shear layer. With highly distorted grids associated with a large deformation of the free surface, remeshing becomes inevitable. The remeshing-based method is referred to as arbitrary Lagrangian–Eulerian (ALE) method. In the ALE method, the flow information in the new grid is transferred from the old one. Since Hirt *et al.* [3] introduced the ALE method, it has been succeedingly ameliorated and modified by a number of researchers in many aspects, making it an attractive choice.

Several researchers applied moving-grid approaches to the free surface flow problems with the finite element method. Güler *et al.* [4] suggested algorithms based on space–time finite element formulation and applied their model to two-dimensional (2D) and three-dimensional (3D) free surface problems. In their approach free surface height was determined by kinematic free surface boundary condition, which also required streamline upwind/Petrov–Galerkin (SUPG) stabilized formulation. Sung *et al.* [5] proposed an ALE finite element approach also based on SUPG stabilization and applied it to solitary wave propagation and run-up on a vertical wall.

On the other hand, the fixed-grid method can be classified into the surface-tracking method and the surface-capturing method. Both methods employ a fixed stationary grid covering the liquid and gas regions. In the surface-tracking method, overlapping interface grid cells or predefined markers explicitly identify and track the free surface. The cells or markers in each cell are advected in the velocity field calculated by interpolation (with appropriate weights) from the velocities in the adjacent grid points. The marker and cell (MAC) method of Harlow and Welch [6] belongs to the surface tracking method. In the surface-capturing method, there is no explicit 'flag' to identify the free surface; the free surface is implicitly captured by a contour of certain scalar functions, such as density, phase field function, and zero level set.

The volume of fluid (VOF) method has enjoyed considerable popularity since its introduction by Hirt and Nichols [7] as a generalization and improvement of MAC. In this method, free surface is represented on fixed grids using a fractional fluid volume in a cell (control volume). The fluid volume fraction then is advected by the local velocity and reconstructed in terms of value of the volume fraction itself. The reconstruction procedure however is mainly a geometric operation in which non-physical interface breakup may occur and fluid parcels may be unrealistically merged into the interface. Recently, Kim and Lee [8] applied the VOF method to two-phase air–water free surface problem in the framework of SUPG finite element method.

The popular surface-capturing method is the level set method (LSM) devised by Osher and Sethian [9]. LSM has been applied widely in a variety of fields, such as incompressible fluid mechanics, combustion, and solidification. In the LSM, a smooth level set function $\phi(\mathbf{x}, t)$, defined as a signed distance function to the interface, represents the interface with a line (2D) or a surface (3D) at the zero level set $\phi(\mathbf{x}, t) = 0$ [10]. Then, the level sets are advected by the local velocity field and redistanced (reinitialized) as a signed distance to the interface. While increase of grid resolution is needed at the interface in other numerical approaches, the interface in LSM can be captured at any time by locating the zero level set. By taking advantage of the smoothness of the level set function, LSM handles topological merging, breaking and even self-intersecting of interfaces in a natural way. Basic information on the interface, such as location, orientation and curvature, can be obtained with ease by examining the zero level set, which provides convenience of estimating surface tension. As in other numerical methods, surface tension can be either diffused over the interface as a δ-function-like volume force in the momentum equations [11] or exactly treated as a jump condition incorporated in the pressure-Poisson equation [12]. Another advantage of LSM is that it can be extended from 2D to 3D in a straightforward manner, which is not in many other algorithms.

Some researchers have applied LSM to incompressible flow in the finite element framework. Quecedo and Pastor [13] simulated two-phase incompressible flow based on the characteristic Galerkin method [14]. Due to the explicit nature of their scheme, the different optimal time steps for momentum equations and level set equations must be determined. Chessa and Belytschko [15] applied the extended finite element method (XFEM) to 2D two-phase immiscible flow problems. The discontinuity in the derivative of the velocity field is enriched by an extended shape function whose gradient is discontinuous across the immiscible fluid interface. Since the discontinuities at the interface are tracked and enriched throughout whole calculation, the XFEM approach [15] can be classified as surface-tracking method. Both approaches [13, 15] employed Chorin's fractional-step algorithm [16] in their explicit discretization of Navier–Stokes equations in characteristic Galerkin formulation, which provided appropriate stabilization.

The objective of the paper is to present a new numerical method that couples the incompressible Navier–Stokes equations with LSM in the finite element framework for study of free surface flows. The method has two new features. One feature is that the implicit characteristic Galerkin scheme is employed to stabilize undesirable oscillations usually observed in convection-dominated problems without resorting to the ENO schemes. It is noteworthy that the ENO schemes have been employed in the finite volume approach for level set reinitialization, which can hinder the efficiency of the scheme due to use of 'if' conditional statements. The second feature is that the governing differential equations are numerically integrated with a fractional four-step method, which guarantees second-order discretization accuracy without special treatment on the boundary condition for the intermediate velocity, unlike other fractional three-step methods. The level set equations of evolution and reinitialization are validated with benchmark cases, including a stationary circle, a rotating slotted disk and stretching of a circular fluid. We then apply and validate the numerical code in several benchmark problems, e.g. a travelling solitary wave and 2D/3D broken dams without and with a square column. The case of the 3D broken dam over a square column is to demonstrate the geometric flexibility of the current method.

This paper is organized as follows. Section 2 describes the mathematical model of the two-phase flow system, the coupling of Navier–Stokes equations with LSM, and the

reinitialization procedure for the level set function. Section 3 details the characteristic Galerkin implementation of level set evolution and reinitialization equations in a weighted integral statement. Section 4 presents the time integration of the incompressible Navier–Stokes equations. Section 5 first examines vortex decay to evaluate the order of accuracy of the Navier–Stokes solver. Then the benchmark cases of Zalesak's disk and a fluid element stretched in a swirling deformation velocity field are simulated for validation of the level set schemes. Finally, the coupled system is applied to the problems of free surface flows.

2. MATHEMATICAL MODEL

2.1. Level set representation of two-phase flows

In the level set method, the free surface is identified as a zero level set, i.e. $\phi(\mathbf{x},t)=0$. The level set function is advected by solving the level set evolution equation

$$\frac{\partial\phi}{\partial t}+\mathbf{u}\cdot\nabla\phi=0 \tag{1}$$

where $\mathbf{u}$ is the fluid velocity. The free surface motion is implicitly represented by the propagation of the zero level set in the equation. With the level set function available, the approach of a volume force by Brackbill *et al.* [17] and Unverdi and Tryggvason [18] is employed to update the fluid properties, such as density and viscosity, and distribute the surface tension smoothly over a thin transition zone.

The level set ϕ is initialized as a signed distance function, which is zero at the free surface, negative in the air region, and positive in the water region. To have a smooth transition of fluid properties from one fluid to the other, the interface region is assumed to be of finite thickness, which satisfies mathematically $|\phi|\leqslant\varepsilon$, where ε is typically one or two grid distances. Thus, the thickness of interface is 2ε. Through the smoothed Heaviside function $H(\phi)$ [11]

$$H(\phi)=\begin{cases}0 & \text{if } \phi<-\varepsilon\\ \dfrac{1}{2}\left[1+\dfrac{\phi}{\varepsilon}+\dfrac{1}{\pi}\sin\left(\dfrac{\pi\phi}{\varepsilon}\right)\right] & \text{if } |\phi|\leqslant\varepsilon\\ 1 & \text{if } \phi>\varepsilon\end{cases} \tag{2}$$

the density and kinematic viscosity are computed by

$$\begin{aligned}\rho(\phi)&=\rho_{\mathrm{g}}+(\rho_{\mathrm{l}}-\rho_{\mathrm{g}})H(\phi)\\ \nu(\phi)&=\nu_{\mathrm{g}}+(\nu_{\mathrm{l}}-\nu_{\mathrm{g}})H(\phi)\end{aligned} \tag{3}$$

where the subscripts g and l denote gas and liquid, respectively.

2.2. Coupling of Navier–Stokes equations with level set function

To couple with the LSM discussed in the previous section, the incompressible Navier–Stokes equations in the Cartesian coordinate system are modified with variable density and

viscosity

$$\frac{\partial u_i}{\partial x_i} = 0 \tag{4}$$

$$\frac{\partial u_i}{\partial t} + u_j \frac{\partial u_i}{\partial x_j} = -\frac{1}{\rho}\frac{\partial p}{\partial x_i} + g_i + \frac{\partial}{\partial x_j}\left(\nu \frac{\partial u_i}{\partial x_j}\right) \tag{5}$$

where u_i is the velocity component and g_i is the gravitational acceleration in the i-direction. Here the surface tension force can be modelled as in Reference [19] and is omitted for simplicity.

2.3. Reinitialization of level set function

The numerical solution of the level set evolution equation (1) does not guarantee that the level set ϕ remains a signed distance function. A reinitialization (or redistancing) procedure for ϕ must be carried out to ensure $|\nabla\phi| = 1$. The approach of Sussman *et al.* [11] that solves the following nonlinear partial differential equation to steady state (from $\tau = 0$ to $\tau = \tau_{\text{steady}}$) is employed

$$\frac{\partial \psi}{\partial \tau} + s(\psi_0)(|\nabla\psi| - 1) = 0 \tag{6}$$

$$\psi_0(\mathbf{x}, \tau = 0) = \phi(\mathbf{x}, t) \tag{7}$$

where $\psi(\mathbf{x}, \tau)$ shares the same zero level set with $\phi(\mathbf{x}, t)$, τ is pseudo time, and $s(\psi_0)$ is the smoothed sign function defined as [20]

$$s(\psi_0) = \frac{\psi_0}{\sqrt{\psi_0^2 + (|\nabla\psi_0|\,\varepsilon)^2}} \tag{8}$$

where ε is usually one grid length. The initial condition to Equation (6) is Equation (7). At steady state, the transient term of Equation (6) is gone, the redistanced function ψ then would satisfy $|\nabla\psi| = 1$. The level set function, ϕ, is subsequently recovered by

$$\phi(\mathbf{x}, t) = \psi(\mathbf{x}, \tau_{\text{steady}}) \tag{9}$$

Equation (6) can be recast as a nonlinear hyperbolic equation.

$$\frac{\partial \psi}{\partial \tau} + \mathbf{c} \cdot \nabla\psi = s(\psi_0) \tag{10}$$

where

$$\mathbf{c} = s(\psi_0)\frac{\nabla\psi}{|\nabla\psi|} \tag{11}$$

Since $\mathbf{c}$ is the characteristic velocity pointing outward from the free surface, reinitialization always starts from the zero level set surface, i.e. the free surface. The accurate ϕ is only needed within the transition (interface) zone. Therefore, $\varepsilon/\Delta\tau$ iteration steps would be enough for practical application of reinitialization. The solution procedure is summarized in Figure 1.

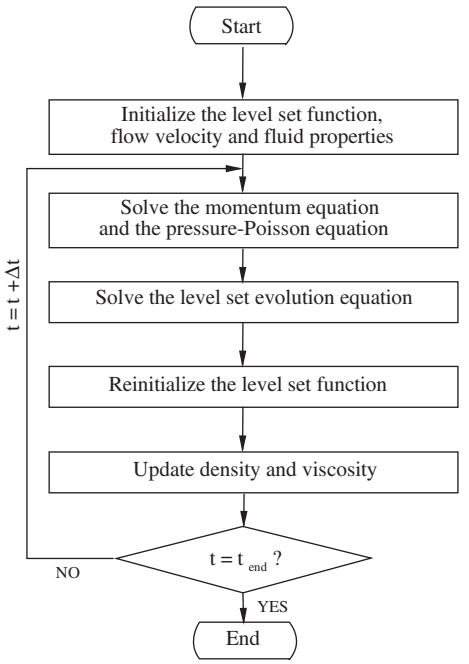

Figure 1. Flow chart of level set calculation.

3. CHARACTERISTIC GALERKIN APPROXIMATION

Since standard Galerkin discretization leads to the central difference approximation of differential operators, Galerkin approximations to the convection equations usually suffer instability problems. Among various techniques to improve stability, streamline upwind Petrov–Galerkin, Taylor–Galerkin [21] and characteristic Galerkin [14] schemes have gained some popularity. The characteristic Galerkin scheme discretizes the original equation in time along the characteristic before applying the spatial discretization. It can be implemented in the framework of standard Galerkin finite element formulation.

The implicit characteristic Galerkin approximation of Equation (1) begins with temporal discretization of ϕ along the characteristic and, then applies local Taylor series expansion to locate the origin of the characteristic at time step $n+\frac{1}{2}$ [22]:

$$\phi^{n+(1/2)} - \phi^{n-(1/2)} = -\Delta t u_i^n \frac{\partial \phi^{n-(1/2)}}{\partial x_i} + \frac{\Delta t^2}{4}\left[u_i^n \frac{\partial}{\partial x_i}\left(u_j^n \frac{\partial \phi^{n-(1/2)}}{\partial x_j}\right) + u_i^n \frac{\partial}{\partial x_i}\left(u_j^n \frac{\partial \phi^{n+(1/2)}}{\partial x_j}\right)\right] + O(\Delta t^3) \tag{12}$$

Suppose that the domain Ω is discretized into an appropriate collection of finite elements. The Galerkin approximation is to find an approximate solution of the following form in a

finite dimensional subspace H^h of the Sobolev space on the spatial domain Ω:

$$\phi = \mathbf{N}^{\mathrm{T}}\boldsymbol{\Phi} \tag{13}$$

where $\mathbf{N}^{\mathrm{T}} = \{N^1, N^2, \ldots, N^{n_e}\}$ is a $(1 \times n_e)$ vector of linear interpolation functions of the element Ω^e, the superscript $(\cdot)^{\mathrm{T}}$ denotes the transpose operation, and n_e is the number of nodal points in an element. $\boldsymbol{\Phi}$ represents a $(n_e \times 1)$ vector of unknown level set functions.

Application of the Galerkin approximation to Equation (12) yields

$$\begin{aligned}
&\left(\int_{\Omega^e} \mathbf{N}\mathbf{N}^{\mathrm{T}}\,\mathrm{d}\Omega\right)(\boldsymbol{\Phi}^{n+(1/2)} - \boldsymbol{\Phi}^{n-(1/2)}) \\
&\quad = -\Delta t \int_{\Omega^e} \mathbf{N} u_i^n \frac{\partial \phi^{n-(1/2)}}{\partial x_i}\,\mathrm{d}\Omega \\
&\qquad + \frac{\Delta t^2}{4} \underbrace{\int_{\Omega^e} \mathbf{N} u_i^n \frac{\partial}{\partial x_i}\left(u_j^n \frac{\partial \phi^{n-(1/2)}}{\partial x_j} + u_j^n \frac{\partial \phi^{n+(1/2)}}{\partial x_j}\right)\mathrm{d}\Omega}_{\mathbf{D}}
\end{aligned} \tag{14}$$

Integrating the second term $\mathbf{D}$ on the right-hand side (RHS) of Equation (14) by parts, applying the divergence theorem of Gauss, and enforcing the continuity equation yield

$$\mathbf{D} = -\int_{\Omega^e} u_i^n \frac{\partial \mathbf{N}}{\partial x_i} u_j^n \left(\frac{\partial \phi^{n-(1/2)}}{\partial x_j} + \frac{\partial \phi^{n+(1/2)}}{\partial x_j}\right)\mathrm{d}\Omega + \int_{\Gamma^e} \mathbf{N} n_i u_i^n u_j^n \left(\frac{\partial \phi^{n-(1/2)}}{\partial x_j} + \frac{\partial \phi^{n+(1/2)}}{\partial x_j}\right)\mathrm{d}\Gamma \tag{15}$$

where Γ^e denotes the surface of elements and n_i is the unit vector outward normal to Γ^e. Equation (14) then can be recast as

$$\begin{aligned}
&\left(\int_{\Omega^e} \mathbf{N}\mathbf{N}^{\mathrm{T}}\,\mathrm{d}\Omega + \frac{\Delta t^2}{4}\int_{\Omega^e} u_i^n u_j^n \frac{\partial \mathbf{N}}{\partial x_i}\frac{\partial \mathbf{N}^{\mathrm{T}}}{\partial x_j}\,\mathrm{d}\Omega - \frac{\Delta t^2}{4}\int_{\Gamma^e} n_i u_i^n u_j^n \mathbf{N}\frac{\partial \mathbf{N}^{\mathrm{T}}}{\partial x_j}\,\mathrm{d}\Gamma\right) \\
&\quad \cdot (\boldsymbol{\Phi}^{n+(1/2)} - \boldsymbol{\Phi}^{n-(1/2)}) \\
&\quad = -\Delta t \int_{\Omega^e} \mathbf{N} u_i^n \frac{\partial \phi^{n-(1/2)}}{\partial x_i}\,\mathrm{d}\Omega - \frac{\Delta t^2}{2}\int_{\Omega^e} u_i^n u_j^n \frac{\partial \mathbf{N}}{\partial x_i}\frac{\partial \phi^{n-(1/2)}}{\partial x_j}\,\mathrm{d}\Omega \\
&\qquad + \frac{\Delta t^2}{2}\int_{\Gamma^e} n_i u_i^n u_j^n \mathbf{N}\frac{\partial \phi^{n-(1/2)}}{\partial x_j}\,\mathrm{d}\Gamma
\end{aligned} \tag{16}$$

The terms of surface integrals cancel out in the interior of the domain Ω. For the no-slip wall and at the inlet and outlet with zero gradient of ϕ, the surface integral may be omitted.

For the reinitialization step, let $\mathbf{c} = c_i$ and $s(\psi_0) = s_0$ in Equation (10) and the distance function ψ is approximated by

$$\psi = \mathbf{N}^{\mathrm{T}}\boldsymbol{\Psi} \tag{17}$$

where $\boldsymbol{\Psi}$ represents a set of unknown distance functions.

Implicit characteristic Galerkin approximation of Equation (10) yields

$$\left(\int_{\Omega^e} \mathbf{N}\mathbf{N}^{\mathrm{T}}\,\mathrm{d}\Omega\right)(\boldsymbol{\Psi}^{m+1}-\boldsymbol{\Psi}^{m}) = \Delta\tau\int_{\Omega^e}\mathbf{N}\left(s_0 - c_i^m\frac{\partial\psi^m}{\partial x_i}\right)\mathrm{d}\Omega + \frac{\Delta\tau^2}{4}\int_{\Omega^e}\mathbf{N}c_i^m\frac{\partial}{\partial x_i}\left(c_j^m\frac{\partial\psi^m}{\partial x_j}\right)\mathrm{d}\Omega + \frac{\Delta\tau^2}{4}\int_{\Omega^e}\mathbf{N}c_i^{m+1}\frac{\partial}{\partial x_i}\left(c_j^{m+1}\frac{\partial\psi^{m+1}}{\partial x_j}\right)\mathrm{d}\Omega \tag{18}$$

where m is the time index used in the reinitialization step. Use of the relationships of

$$c_i\frac{\partial\psi}{\partial x_i} = s_0\frac{\nabla\psi}{|\nabla\psi|}\nabla\psi = s_0|\nabla\psi| \tag{19}$$

and

$$c_i s_0|\nabla\psi| = s_0\frac{\nabla\psi}{|\nabla\psi|}s_0|\nabla\psi| = \nabla\psi \tag{20}$$

yields

$$\left(\int_{\Omega^e}\mathbf{N}\mathbf{N}^{\mathrm{T}}\,\mathrm{d}\Omega + \frac{(\Delta\tau)^2}{4}\int_{\Omega^e}\frac{\partial\mathbf{N}}{\partial x_i}\frac{\partial\mathbf{N}^{\mathrm{T}}}{\partial x_i}\,\mathrm{d}\Omega - \frac{\Delta\tau^2}{4}\int_{\Gamma^e}\mathbf{N}\frac{\partial\mathbf{N}^{\mathrm{T}}}{\partial x_i}n_i\,\mathrm{d}\Gamma\right)(\boldsymbol{\Psi}^{m+1}-\boldsymbol{\Psi}^{m})$$
$$= \Delta\tau\int_{\Omega^e}\mathbf{N}s_0(1-|\nabla\psi^m|)\,\mathrm{d}\Omega - \frac{(\Delta\tau)^2}{2}\int_{\Omega^e}\frac{\partial\mathbf{N}}{\partial x_i}\frac{\partial\psi^m}{\partial x_i}\,\mathrm{d}\Omega + \frac{(\Delta\tau)^2}{2}\int_{\Gamma^e}\mathbf{N}\frac{\partial\psi^m}{\partial x_i}n_i\,\mathrm{d}\Gamma$$
$$\underbrace{-\frac{(\Delta\tau)^2}{4}\int_{\Omega^e}\mathbf{N}s_0\left(|\nabla\psi^{m+1}|\frac{\partial c_i^{m+1}}{\partial x_i} + |\nabla\psi^m|\frac{\partial c_i^m}{\partial x_i}\right)\mathrm{d}\Omega}_{\mathbf{A}} \tag{21}$$

Since $\partial c_i^m/\partial x_i$ and $\partial c_i^{m+1}/\partial x_i$ are the second-order spatial derivatives of the distance function ψ, the term **A** in Equation (21) can be omitted if linear interpolation functions are used.

4. NUMERICAL INTEGRATION OF NAVIER–STOKES EQUATIONS

The most prominent strength of the finite element method is its geometric flexibility. In this study, the implicit characteristic Galerkin finite element method is employed for the time integration of incompressible Navier–Stokes equations.

4.1. Fractional four-step method

The fractional four-step method by Choi *et al.* [23] is applied to solve the continuity and momentum equations, Equations (4) and (5). The four-step method does not require any special treatment on the boundary conditions of the intermediate velocity with preserving

second-order accuracy. The continuity equation is enforced by solving a pressure-Poisson equation (24). The implicit characteristic Galerkin approximation of these equations reads:

1. Momentum Predictor

$$\frac{\hat{u}_i - u_i^n}{\Delta t} + u_j^n \frac{\partial u_i^n}{\partial x_j} = -\frac{1}{\rho^{n+(1/2)}} \frac{\partial p^{n-(1/2)}}{\partial x_i} + g_i + \frac{1}{2}\left[\frac{\partial}{\partial x_j}\left(v\frac{\partial u_i^n}{\partial x_j}\right) + \frac{\partial}{\partial x_j}\left(v\frac{\partial \hat{u}_i}{\partial x_j}\right)\right] + \frac{\Delta t}{4}\left[u_k^n \frac{\partial}{\partial x_k}\left(u_j^n \frac{\partial u_i^n}{\partial x_j}\right) + \hat{u}_k \frac{\partial}{\partial x_k}\left(\hat{u}_j \frac{\partial \hat{u}_i}{\partial x_j}\right)\right] + \frac{\Delta t}{2} u_k^n \frac{\partial}{\partial x_k}\left(\frac{1}{\rho^{n+(1/2)}} \frac{\partial p^{n-(1/2)}}{\partial x_i}\right) \tag{22}$$

2. First Corrector

$$\frac{u_i^* - \hat{u}_i}{\Delta t} = \frac{1}{\rho^{n+(1/2)}} \frac{\partial p^{n-(1/2)}}{\partial x_i} \tag{23}$$

3. Pressure-Poisson Equation

$$\frac{\partial}{\partial x_i}\left(\frac{1}{\rho^{n+(1/2)}} \frac{\partial p^{n+(1/2)}}{\partial x_i}\right) = \frac{1}{\Delta t} \frac{\partial u_i^*}{\partial x_i} \tag{24}$$

4. Second Corrector

$$\frac{u_i^{n+1} - u_i^*}{\Delta t} = -\frac{1}{\rho^{n+(1/2)}} \frac{\partial p^{n+(1/2)}}{\partial x_i} \tag{25}$$

where the implicit nonlinear convection stabilizing term on the RHS of Equation (22) is treated by Picard iterative method.

4.2. Finite element formulation for pressure-Poisson equation

The pressure-Poisson equation is solved using the procedure of Choi *et al.* [23] for mass conservation. Because the current approach adopts an equal-order velocity formulation, the order of interpolation functions for the continuity equation is the same as those of the momentum equations. Consider the approximation of pressure

$$p = \mathbf{N}^{\mathrm{T}}\mathbf{P} \tag{26}$$

$\mathbf{U}$ and $\mathbf{P}$ are $(n_e \times 1)$ vectors of redefined nodal particle distribution functions. The standard Galerkin finite approximation employs interpolation functions as weight function, thus resulting in the weak form of the continuity equation (4)

$$\int_{\Omega^e} \mathbf{N} \frac{\partial u_i^{n+1}}{\partial x_i} \, \mathrm{d}\Omega = 0 \tag{27}$$

Applying the divergence theorem, Equation (27) can be written as

$$\int_{\Omega^e} \frac{\partial \mathbf{N}}{\partial x_i} u_i^{n+1} \, \mathrm{d}\Omega = \int_{\Gamma^e} \mathbf{N} u_i^{n+1} n_i \, \mathrm{d}\Gamma \tag{28}$$

Substitution of Equation (25) for u_i^{n+1} yields the pressure-Poisson equation

$$\left(\Delta t \int_{\Omega^e} \frac{\partial \mathbf{N}}{\partial x_i} \frac{1}{\rho} \frac{\partial \mathbf{N}^{\mathrm{T}}}{\partial x_i} \mathrm{d}\Omega\right) \mathbf{P} = \int_{\Omega^e} \frac{\partial \mathbf{N}}{\partial x_i} u_i^* \, \mathrm{d}\Omega - \int_{\Gamma^e} \mathbf{N} u_i^{n+1} n_i \, \mathrm{d}\Gamma \tag{29}$$

As pointed out by Choi *et al.* [23], the unknown velocity u_i^{n+1} at the boundary nodes on the RHS of Equation (29) can be replaced by $\hat{u}$ without violating second-order accuracy. This can be easily verified by Equations (23) and (25)

$$\begin{aligned} \hat{u}_i &= u_i^{n+1} + \frac{\Delta t}{\rho^{n+(1/2)}} \frac{\partial (p^{n+(1/2)} - p^{n-(1/2)})}{\partial x_i} \\ &= u_i^{n+1} + O(\Delta t^2) \end{aligned} \tag{30}$$

The resulting system of linear equations are solved by the conjugate gradient method. Since the characteristic Galerkin scheme has an accuracy of order two, it will be verified later in Section 5.1.1.

5. COMPUTATIONAL RESULTS

In this section, several benchmark problems are simulated for code verification and validation. Because the coupled system consists of Navier–Stokes solver and level-set method, each of them shall be evaluated separately prior to assessing the coupled system. The single-phase decaying vortex problem is first considered in Section 5.1. The order of accuracy of the scheme is verified by comparison of numerical and analytical solutions. In Section 5.2 the level-set evolution and reinitialization solutions are examined. In particular, they are compared with those obtained from the level-set finite-volume method of Yue *et al.* [19], who compared different numerical schemes for advection of the level set function in a generalized curvilinear format, including the third-order quadratic upwind interpolation for convective kinematics (QUICK) scheme, and the second- and third-order ENO schemes. In Section 5.3 the coupled two-phase system is validated by solitary wave and broken dam problems without and with a square column.

5.1. Accuracy and discretization errors

5.1.1. Vortex decay. The 2D unsteady vortex decay problem [24, 25] is examined to calculate the discretization errors and estimate the order of accuracy of the scheme for verification. The rate of vortex decay is dependent on the wavenumber and the Reynolds number of the flow. The analytical solutions of the problem read

$$u(x, y, t) = -\cos(kx)\sin(ky)\exp(-2k^2 t/Re) \tag{31}$$

$$v(x, y, t) = \sin(kx)\cos(ky)\exp(-2k^2 t/Re) \tag{32}$$

$$p(x, y, t) = -\tfrac{1}{4}[\cos(2kx) + \cos(2ky)]\exp(-4k^2 t/Re) \tag{33}$$

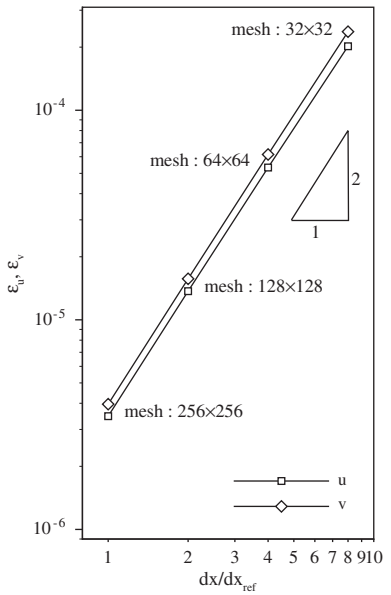

Figure 2. Average error as a function of mesh refinement.

where $0 \leqslant (x, y) \leqslant \pi$, t is time, k is the characteristic wavenumber of the flow field, and Re is the Reynolds number. Discretization errors are obtained by comparing numerical solutions against the above analytical ones. The order of accuracy of the scheme is estimated using the solutions calculated on four systematically refined rectangular meshes: 32×32, 64×64, 128×128 and 256×256, with $k = 1$ and $Re = 1$. It is noteworthy that time steps shall be altered accordingly with meshes to maintain consistent Courant number ($Cr = u_{\max} \Delta t / \Delta x$, where Δt is the time step and Δx is the grid spacing) as in Reference [24] because of the transient nature of the problem. The initial condition is obtained from Equations (31)–(33) at $t = 0$. Time-dependent essential boundary conditions for two velocity components u and v are imposed at every time step based upon Equations (31)–(33). Figure 2 displays the relationship between grid sizes and average errors calculated at $t = 0.15$ s. The slope of the curve confirms that the current scheme is of second-order accuracy.

5.2. *Reinitialization and evolution of level set function*

5.2.1. A stationary circle. Reinitialization is a key procedure in LSM. To verify the implementation of the level set schemes presented in Section 3, the reinitialization procedure is applied to a stationary circle. The level set function is initially assigned with a value of $+0.15$ outside the circle and a value of -0.15 inside the circle. As shown in Figure 3 two types of meshes with a domain size of 100×100 are considered: a uniform mesh and a hybrid mesh. For the hybrid mesh a half of the domain comprises quadrilateral elements, whereas the other half contains triangular elements. The centre of the circle coincides with the centre of the square domain and the radius of the circle is set to 15. Figure 4 exhibits the contours of

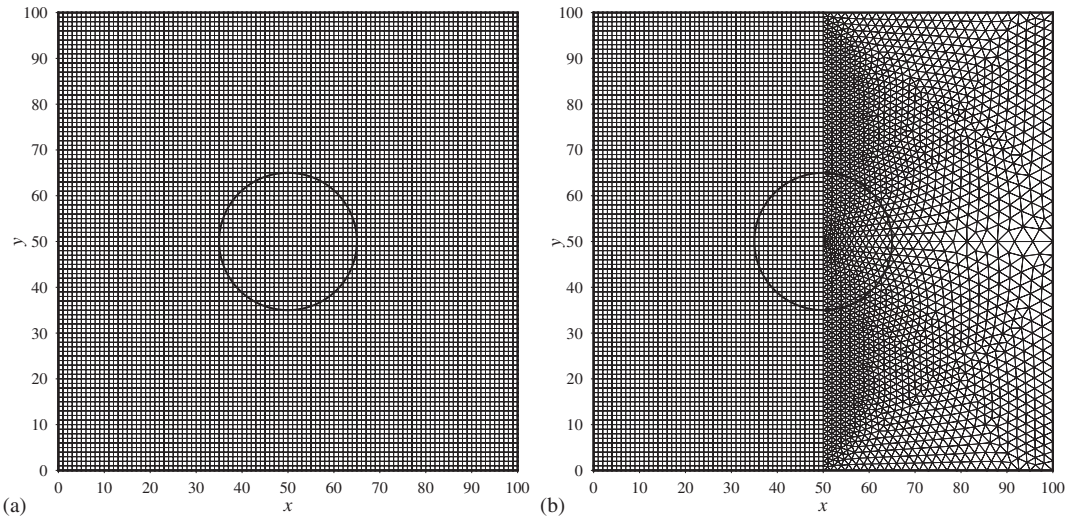

Figure 3. Meshes used for reinitialization test: (a) uniform mesh; and (b) hybrid mesh.

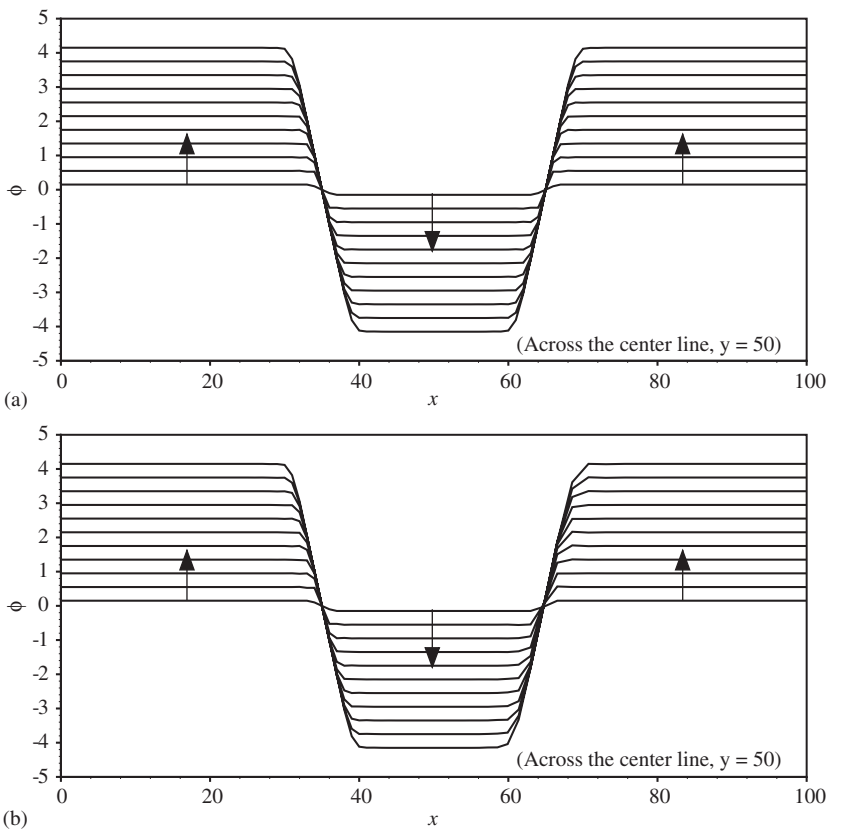

Figure 4. Evolution of level set surface $\phi = 0$ on: (a) uniform mesh; and (b) hybrid mesh.

$\phi = 0$ at ten different time units on the two meshes. ϕ is well redistanced as a signed distance function with increasing time ($|\nabla\phi| = 1$) regardless of mesh type.

5.2.2. Rotation of a slotted disk. Zalesak's problem of a rotating slotted disk [26] has become a benchmark case for testing an advection scheme, in which a slotted solid disk rotates around a centre with a constant angular velocity. We use this problem to measure the diffusive error of the present LSM. Here the slotted disk has a radius of 15 and a slot width of 6. It is initially located at $(50, 75)$ in the domain of size 100×100. The angular velocity Ω is set to 0.01 so that the disk can return to its original position at every 628 time units. The diffusive errors can be evaluated by checking the degree of distortion of the disk boundary. For comparison, we employ three meshes: a uniform mesh of 100×100 square elements, a refined uniform mesh of 200×200 square elements and a triangular mesh of 11 421 nodal points and 22 440 elements. The time step $\Delta t = 0.5$ is used for the refined 200×200 uniform mesh and $\Delta t = 1.0$ for the other two meshes. Because this is a problem of pure advection by the constant angular velocity, a good evolution scheme is expected to adequately preserve the disk geometry without reinitialization.

Figure 5 displays the rotation of a slotted disk at $t = 0, 157, 314, 471$ and 628 s on the three meshes. The half-thickness of the interface is set as $\varepsilon = 2\Delta x$. Table I shows the area errors

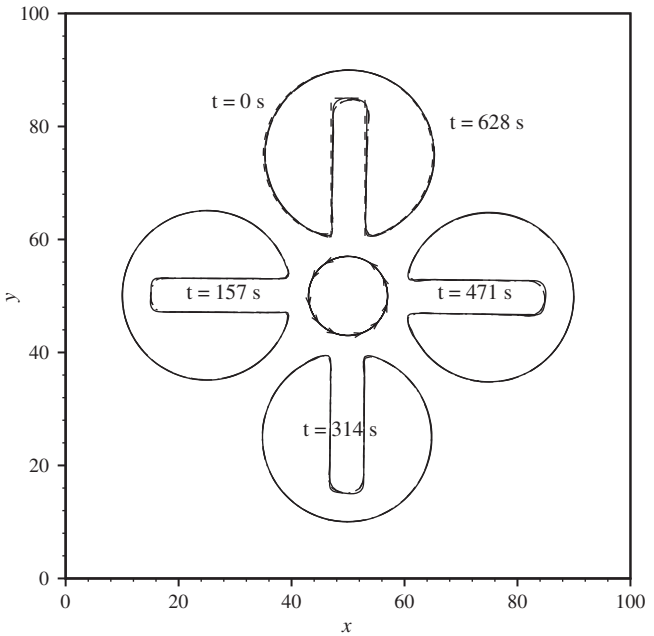

Figure 5. Counter-clockwise rotation of a slotted disk. Dotted line, initial shape; solid lines, uniform 200×200 mesh; dash-dot lines, uniform 100×100 mesh; dash-dot-dot lines, 11 421-node triangular mesh.

Table I. Area error during the rotation of Zalesak's slotted disk.

Mesh	$t = 157$ s	$t = 314$ s	$t = 471$ s	$t = 628$ s
Uniform mesh (100×100)	−0.0100%	−0.0034%	0.0033%	0.0101%
Uniform mesh (200×200)	−0.0030%	−0.0014%	−0.0010%	−0.0015%
Triangular mesh (11 421 points, 22 440 elements)	−0.0025%	0.0008%	0.0073%	0.0133%

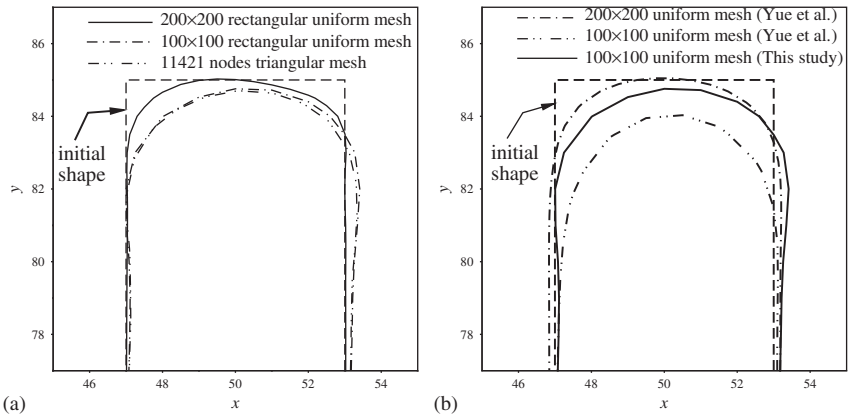

Figure 6. (a) A closed-up view of a slotted disk after a rotation on three different meshes (this study); and (b) comparison with the solution of Yue *et al.* [19] using a 3rd order ENO scheme.

during the revolution. The area error is calculated by

$$\varepsilon_A = \frac{A(t) - A(0)}{A(0)} \times 100(\%) \tag{34}$$

where $A(t) = \int_\Omega H(\phi)\,\mathrm{d}\Omega$ is the total area of fluid at time t, A_0 is the initial area at $t = 0$. Figure 6 is a close-up view at $t = 628$ s of the present study and Yue *et al.* [19], who also tested this problem with the finite volume level set method with a third-order ENO scheme. The aberrations from the original shape in this study are all within one mesh size even though the corners do not remain as sharp as the original ones. The 200×200 fine mesh preserves the original shape much better than two other meshes as expected. The qualitative comparison shows that the performance with a 100×100 mesh is much better than that of Yue *et al.*'s 100×100 mesh and comparable to Yue *et al.*'s 200×200 mesh.

5.2.3. Stretching of a circular fluid. A circular fluid is placed in a swirling deformation flow field within a unit square described by

$$\varphi = \frac{1}{\pi} \sin^2(\pi x) \sin^2(\pi y) \tag{35}$$

where φ is the stream function. The fluid is stretched into a thin filament by the shearing velocity field. This case provides a challenging test for both surface-tracking and surface-

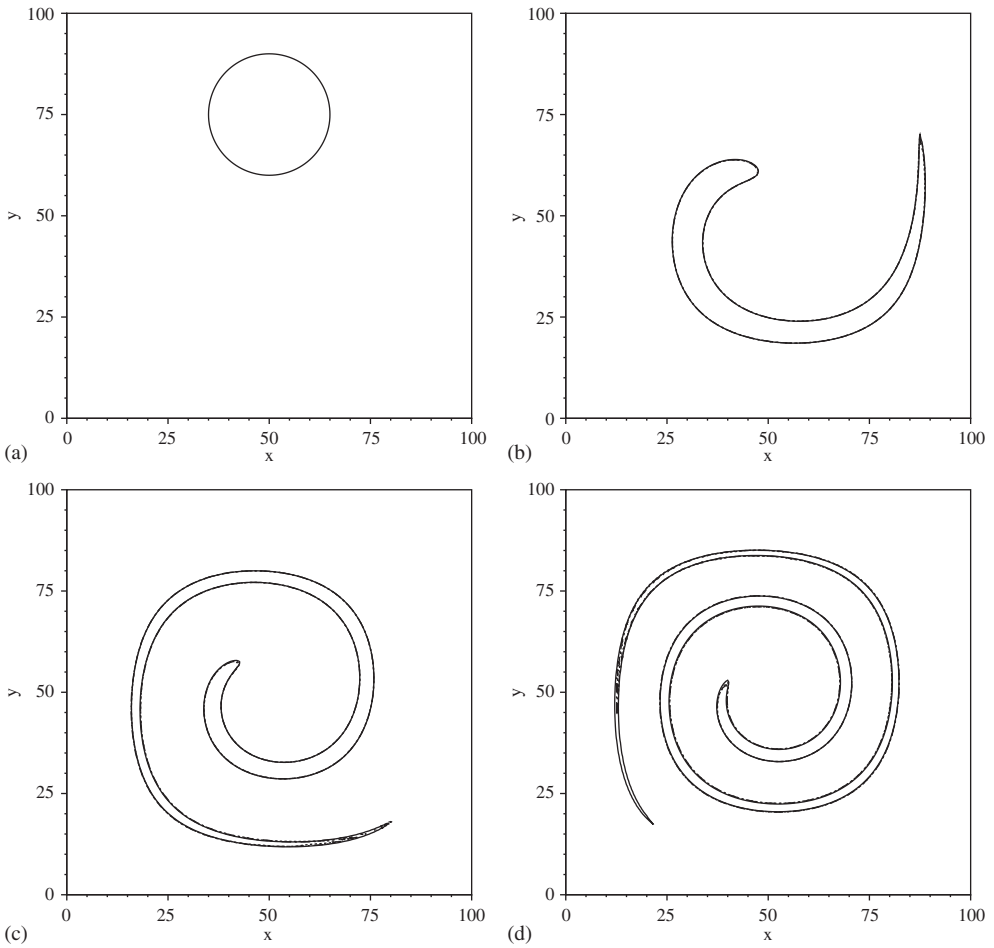

Figure 7. Stretching of a circular fluid element in a swirling deformation flow at $t =$: (a) 0; (b) 100; (c) 200; and (d) 300. Solid lines, uniform 200×200 mesh; dashed line, uniform 100×100 mesh; dash-dot lines, triangular mesh (11 421 points, 22 440 elements).

capturing methods. Rider and Kothe [27] and Rudman [28] employed this problem to evaluate their VOF scheme. The same mesh and domain size as Zalesak's problem are adopted here. The circle is initially centred at $(50, 75)$ with a radius of 15. The solenoidal velocity field becomes

$$u = -\sin^2\left(\frac{\pi x}{100}\right)\sin\left(\frac{\pi y}{50}\right), \quad v = \sin^2\left(\frac{\pi y}{100}\right)\sin\left(\frac{\pi x}{50}\right) \tag{36}$$

Note that a time step of 0.5 is used for the two coarse meshes, and 0.25 for the mesh of 200×200 to maintain a consistent Cr number.

Figure 7 shows the stretching process of the circular fluid element at $t = 0, 100, 200$ and 300s on the two rectangular meshes and triangular mesh. The circular fluid element is torn into

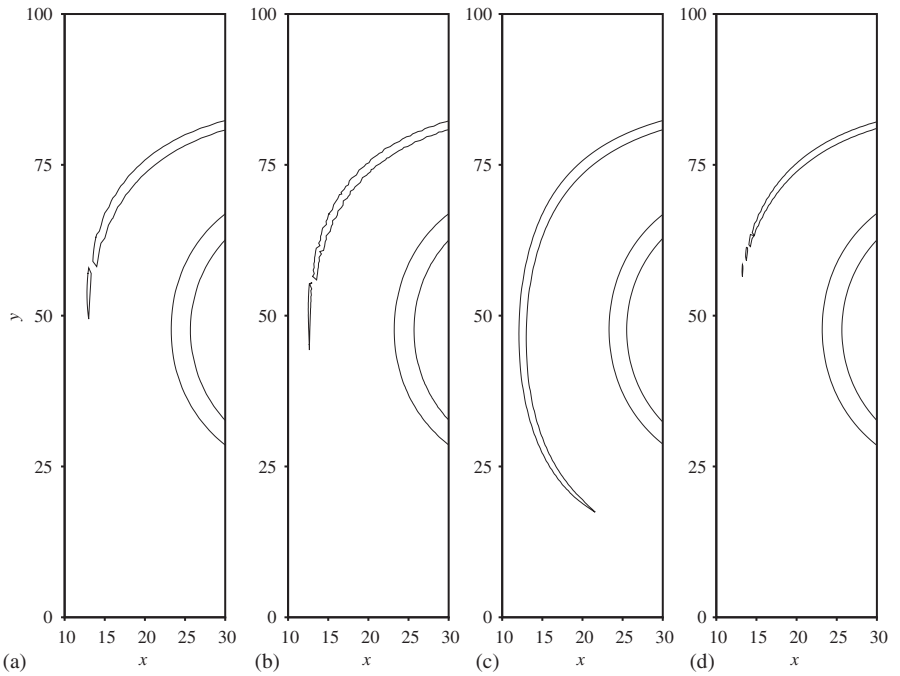

Figure 8. A close-up view of stretched tails at $t = 300$ s on: (a) uniform 100×100 mesh; (b) triangular mesh (11 421 points, 22 440 elements); (c) uniform 200×200 mesh (this study); and (d) uniform 200×200 mesh [19].

a filament by the shearing vortex, and becomes thinner as time proceeds. At $t = 0$ and 100 s the preservation of the fluid element on the three meshes seems indistinguishable. However the tail regions of the fluid filament become different at $t = 200$ and 300 s. Figure 8 further displays the close-up view of the stretched tails at $t = 300$ s on each mesh. The results of 100×100 and triangular meshes at $t = 300$ s show slight breakups, but appear closer to the fine grid solution (Figure 8(c)) as compared with the level set simulation of Yue *et al.* [19] (Figure 8(d)) which was calculated on a 200×200 fine mesh.

For the purpose of evaluating the errors of area preservation and the accuracy of interface advection and deformation, the velocity field expressed by Equation (36) is multiplied by $\cos(\pi t/T)$ and the stretching process is time-reversed according to Leveque [29], where T is the prescribed reversal period. The flow slows down and the fluid is stretched out during $0 < t < T/2$. The flow reverses direction and the fluid is shrunk back during $T/2 < t < T$. The fluid is expected to recover its initial circular shape at $t = T$. Two periods, $T = 250$ and 500, are chosen for comparison. Figure 9 shows that the fluids calculated on all the three meshes recover the circular shape without any significant deformation after a period of $T = 250$ and 500. To quantitatively assess the accuracy of the present LSM, the area errors are calculated. Table II indicates that the area errors of the present LSM are much smaller than those of Yue *et al.* [19]. This test concludes that the current scheme can resolve the stretched interface on the scale of mesh size without bringing any significant distortion.

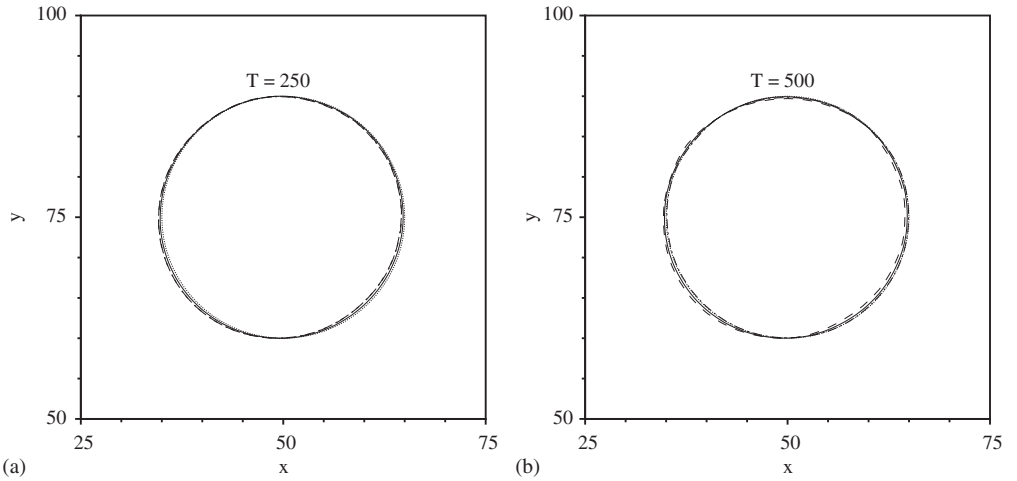

Figure 9. Reversed circular fluid elements after one period $T =$: (a) 250; and (b) 500. Dotted lines, initial contour of the circular fluid; solid lines, uniform 200×200 mesh; dashed lines, uniform 100×100 mesh; dash-dot lines, triangular mesh (11 421 points, 22 440 elements).

Table II. Area error after one period for a circular fluid in the time-reversed swirling deformation flow.

Mesh	Area error ($T = 250$) (%)	Area error ($T = 500$) (%)
Uniform mesh (100×100) [19]	0.687	0.09
Uniform mesh (100×100) (This study)	−0.0478	−0.0349
Non-uniform mesh (100×100) [19]	0.42	−1.635
Uniform mesh (200×200) [19]	0.038	1.36
Uniform mesh (200×200) (This study)	−0.0263	−0.0213
Triangular mesh (11 421 points, 22 440 elements) (This study)	−0.0410	−0.0262

5.3. Benchmark tests of the coupled system

5.3.1. Travelling of a solitary wave. Propagation of a solitary wave is a simple and practical free surface problem, which has been extensively studied experimentally and numerically. Here we aim to examine whether the coupled system can predict the viscous damping characteristics and run-up on a vertical wall of a travelling solitary wave in a channel shown in Figure 10. Let h denote the depth of still water, and the subscripts a and w denote air and water, respectively. The channel size is $20h \times 2h$. The theoretical wave speed $C_w = \sqrt{gh}$ is set to 1.0 m/s, the Reynolds number $Re = C_w h/\nu_w = 5 \times 10^4$, the viscosity ratio $\nu_a/\nu_w = 15$ and the density ratio $\rho_a/\rho_w = 1.2 \times 10^{-3}$. A mesh of 400×59 rectangular elements is used. The mesh sizes are uniform in the x-direction and also uniform within the range $(-0.1, 0.5)$ in the y-direction, then expands to the top and bottom boundaries. The half thickness of interface in Equation (2) is fixed with three mesh size $3(\Delta y)_{\min}$. The Courant number $Cr = C_w \Delta t/(\Delta y)_{\min}$ is set to 1.

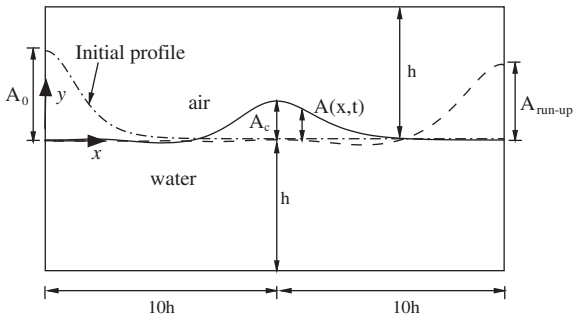

Figure 10. Schematic of the formation, travelling and run-up of a solitary wave in an enclosed channel.

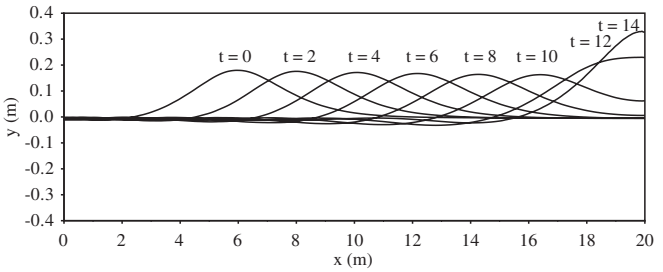

Figure 11. Travelling trains of a solitary wave at selected times.

To generate a solitary wave, one can make use of Laitone's analytical approximation [30]. Here we release an initially still water surface with a Boussinesq profile [31] from the left vertical wall which is in hydrostatic balance

$$A(x,0) = A_0/\cosh^2\left(\frac{\sqrt{3A_0}}{2}x\right) \tag{37}$$

After $t = 6$ s, the wave is assumed to be free from the influence of the left wall boundary and can be considered as a solitary wave. The time is then reset as the initial time ($t = 0$) of the solitary wave propagation. Because of the large density ratio of air and water, the top boundary condition has negligible effects on the motion of the solitary wave, thus no-slip boundary condition is applied there. As for the boundary condition for the level set function ϕ at the wall, we adopt the gradient free condition $\partial\phi/\partial n = \nabla\phi \cdot \mathbf{n} = 0$, where $\mathbf{n}$ is the normal vector of the wall boundary. Figure 11 shows the travelling train of the solitary wave and its run-up on the right vertical wall for the case $A_0/h = 0.4$. To quantitatively assess the accuracy of the current coupled system, nine cases of wave run-ups (run-up is defined as the highest point at the right vertical wall) with different initial wave amplitudes are calculated. The computational results are compared with the experimental data by Chan *et al.* [32] and the numerical result of Yue *et al.* [19] in Figure 12. The A_c in the x-axis of Figure 12 is the amplitude of the solitary wave in the middle of the horizontal distance of the computational

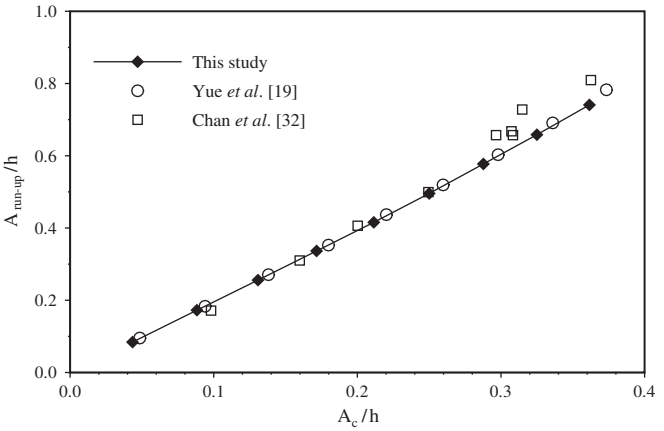

Figure 12. Wave run-up height versus incident wave amplitude.

domain as shown in Figure 10. The agreement between computation and experiment is excellent within $A_c/h < 0.3$. After the value $A_c/h = 0.3$, the experimental data exhibit some scatter. Overall the above results demonstrate that the present coupled system can accurately predict the viscous damping characteristics without introducing undesirable numerical damping effects.

5.3.2. 2D broken dam problem. The collapse of a water column on a rigid horizontal plane is called a broken dam problem. It is used to simulate the abrupt failure of a dam, in which an initially blocked still water column spreads out immediately after the blocking is removed. It has been experimentally studied in detail by Martin and Moyce [33] to investigate the spreading velocity and the falling rate of water columns. The motion of the water was recorded by cine-photography at about 300 frames per second in their experiments. One of their cases, a square water column with length $a = 2\frac{1}{4}$ inch, is examined here to validate the present model. This problem has also been studied numerically by many researchers, e.g. Kelecy and Pletcher [34].

The computational domain is $5a \times 1.25a$ as sketched in Figure 13, being the same as the one employed by Kelecy and Pletcher. Here s and h denote the surge front position and the remaining height of the water column, respectively; they are used to measure the spreading velocity and the falling rate of the water column. The numerical experiments are conducted in a closed container with all wall boundaries on two types of meshes: a uniform mesh of 2500 rectangular elements and a mesh of 5608 triangular elements (Figure 14). The still water column is initially in hydrostatic balance. The time is non-dimensionalized by $t_g = \sqrt{a/g}$ in all the plots.

Figure 15 shows the comparison of the surge fronts between our computations and Martin and Moyce's experiment. Overall the present model predicts the water spreading velocity very well. Figure 16 shows the comparison of the remaining water column height between computation and experiment. They are also in good agreement regardless of meshes.

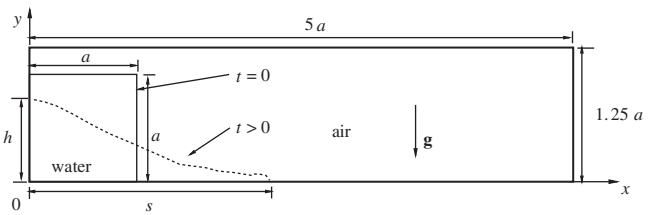

Figure 13. Schematic of a 2D broken dam.

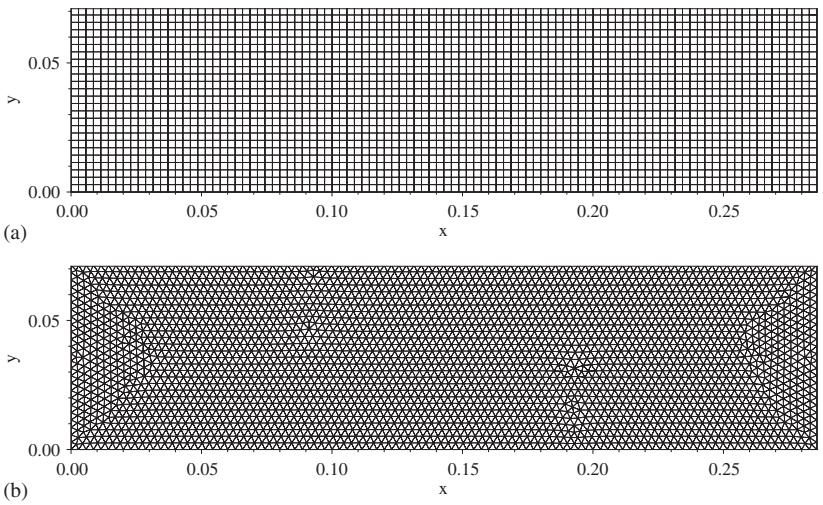

Figure 14. Meshes used in the 2D broken dam simulation: (a) rectangular mesh (2626 nodal points, 2500 ($=100\times25$) square elements); and (b) triangular mesh (2930 nodal points, 5608 triangular elements).

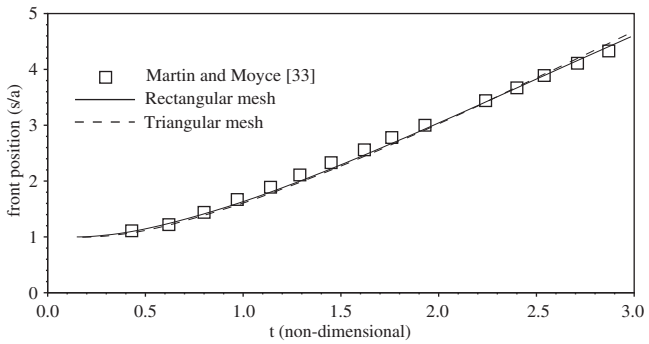

Figure 15. Surge front position s versus non-dimensional time in 2D broken dam simulations.

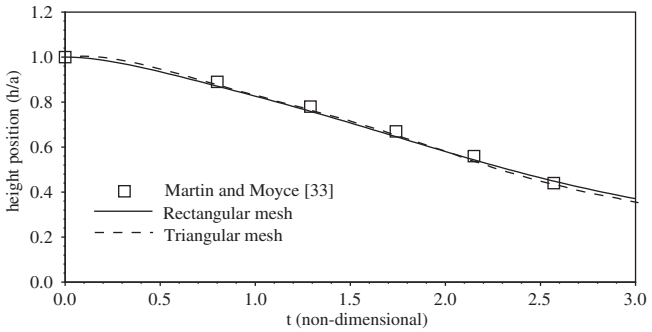

Figure 16. Remaining water column height h versus non-dimensional time in 2D broken dam simulations.

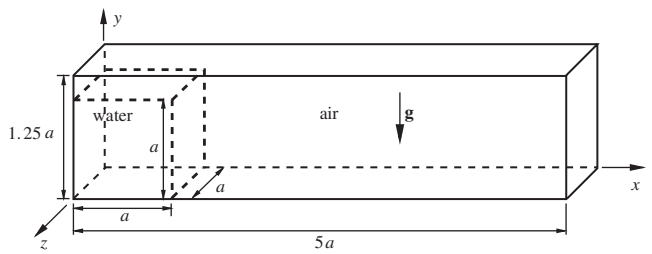

Figure 17. Schematic of a 3D broken dam setup.

5.3.3. 3D broken dam problem. For a more realistic simulation of free surface flow, 3D broken dam problem is tested by the present model. The cubic water column is used for the initial condition (Figure 17). The size of the computational domain is $5a \times a \times 1.25a$ (with $a = 2\frac{1}{4}$ inch) in the x, y, and z directions, respectively. A total of $200 \times 40 \times 50$ hexahedral (brick) uniform elements are used for the simulation. All the boundaries are treated as walls. Figure 18 shows the evolution of free surface and corresponding velocity vector plots. Figures 19 and 20 display the front surge and the remaining height location at the bottom and left wall, respectively. All the variables are non-dimensionalized as in the case of 2D broken dam problem. The results are again in good agreement with the experimental data of Martin and Moyce [33].

5.3.4. 3D broken dam with a square column. The problem of a broken dam over a square column is of practical importance in terms of functional and structural design of hydraulic structures. Figure 21 is a schematic description of the problem. Recently, Gómez-Gesteira and Dalrymple [35] applied the smoothed particle hydrodynamics method to study this problem. As an initial condition the floor is assumed to be covered by a thin layer (1 cm) of water to be consistent with the physical experiment [35]. Only half of the entire domain is needed for simulation owing to the geometric symmetry of the problem. A total of 181 905 nodes and 169 752 hexahedral elements are employed. Figure 22 displays a time sequence of free

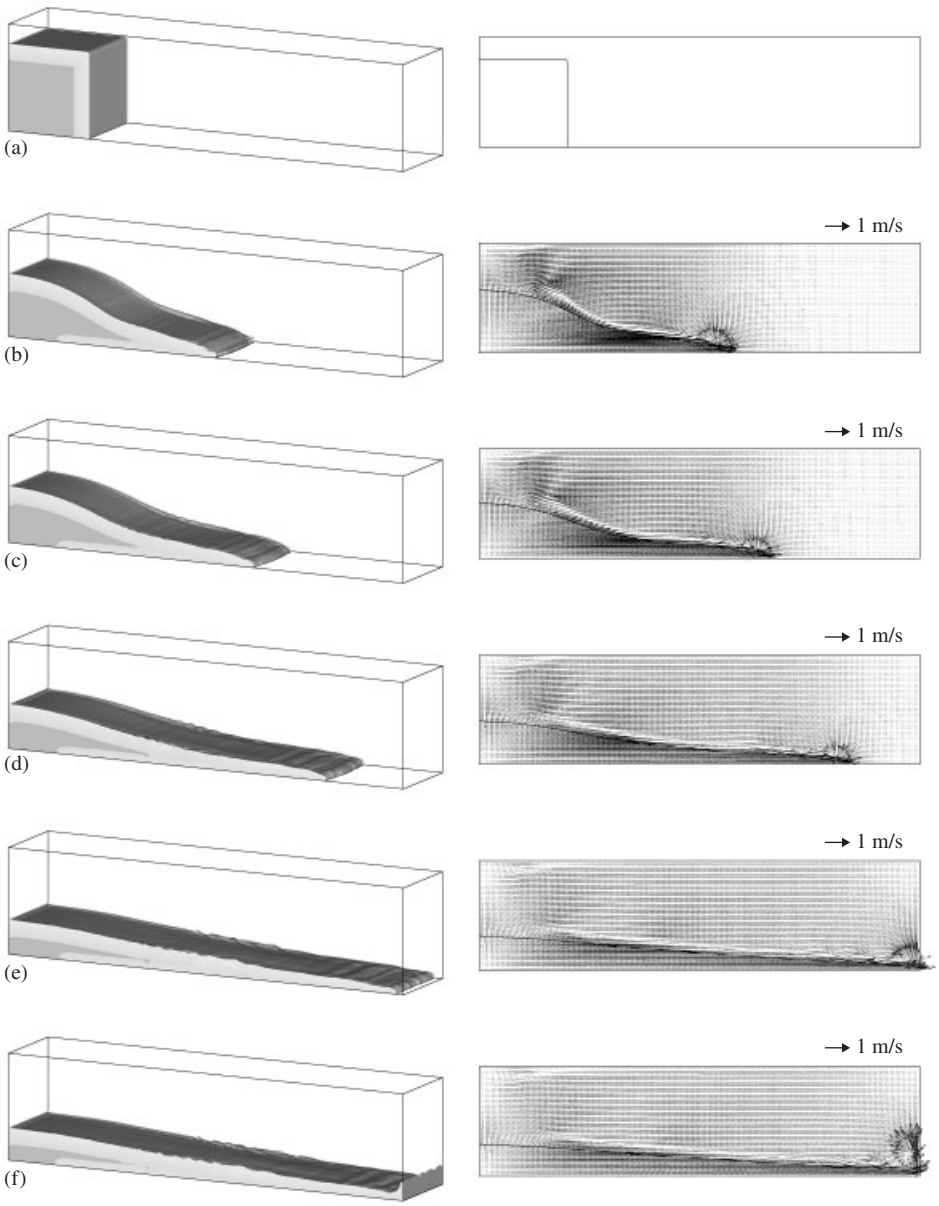

Figure 18. Free surface configuration and velocity vectors in the centre plane of the container at selected (non-dimensionalized) times: (a) $t = 0.000$; (b) $t = 1.481$; (c) $t = 1.788$; (d) $t = 2.369$; (e) $t = 2.950$; and (f) $t = 3.122$.

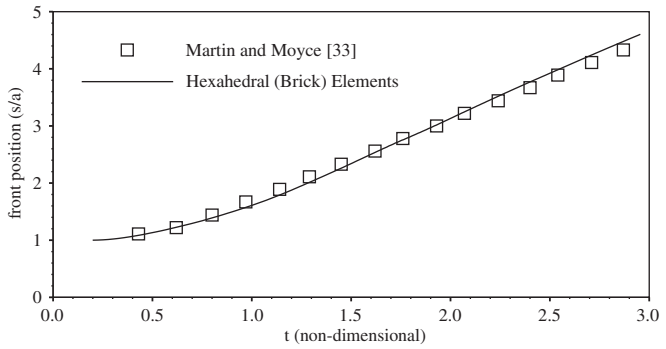

Figure 19. Surge front position s versus non-dimensional time in a 3D broken dam simulation.

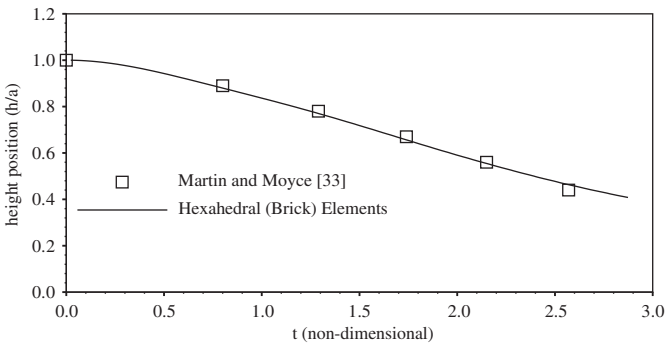

Figure 20. Remaining water column height h versus non-dimensional time in a 3D broken dam simulation.

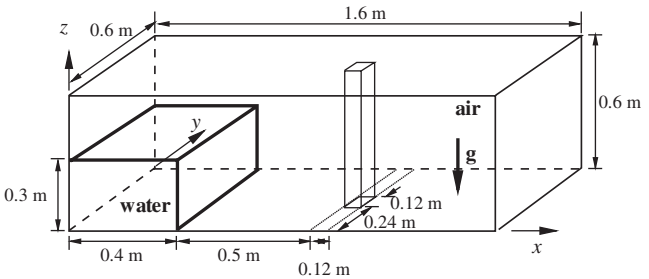

Figure 21. Schematic description of a 3D broken dam over a column.

surface deformation. For a quantitative assessment of the solution, the x velocity component taken at 0.146 m upstream of the centre of the column and 0.026 m off the floor and the force exerted on the column are compared with the experimental data [36]. The force acting on the

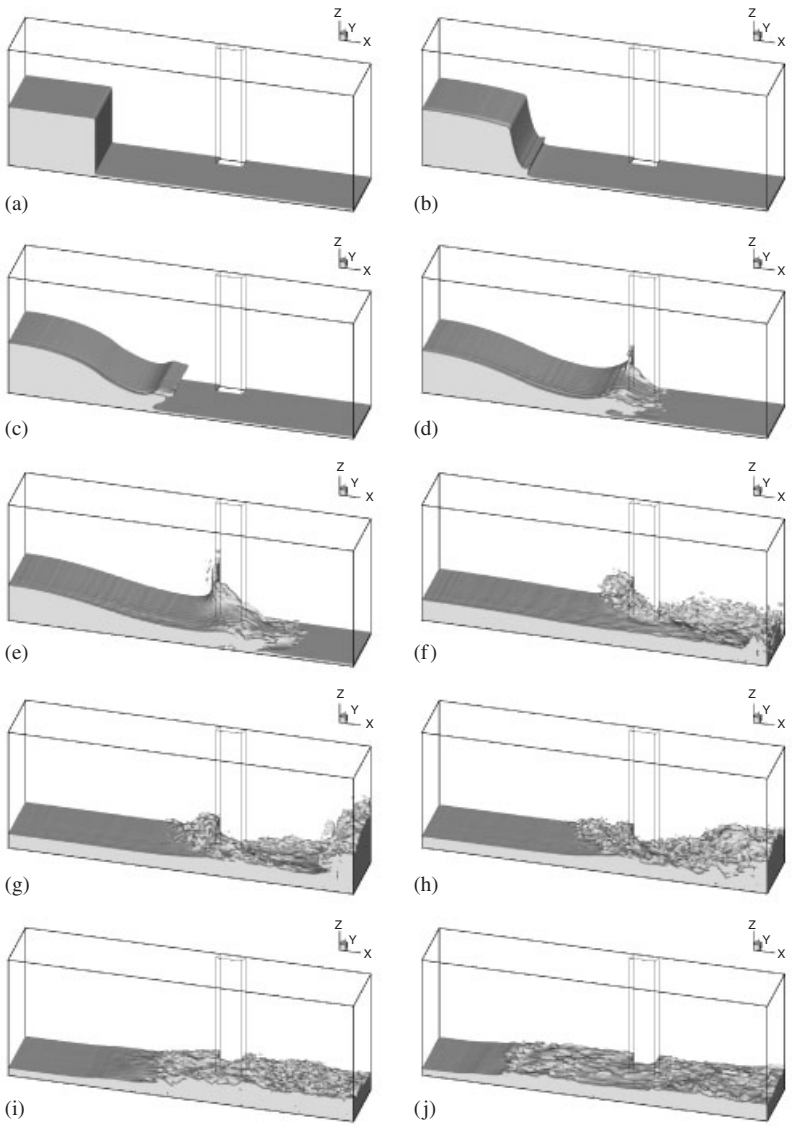

Figure 22. Free surface evolution of a broken dam over a column: (a) $t = 0.000$ s; (b) $t = 0.092$ s; (c) $t = 0.213$ s; (d) $t = 0.332$ s; (e) $t = 0.430$ s; (f) $t = 0.736$ s; (g) $t = 1.006$ s; (h) $t = 1.230$ s; (i) $t = 1.983$ s; and (j) $t = 2.341$ s.

column is calculated by integrating the pressure field on the surface of column. The force in the positive x direction is assumed positive. Figure 23 shows quite reasonable agreement with the experimental data given the complexity of the free surface deformation.

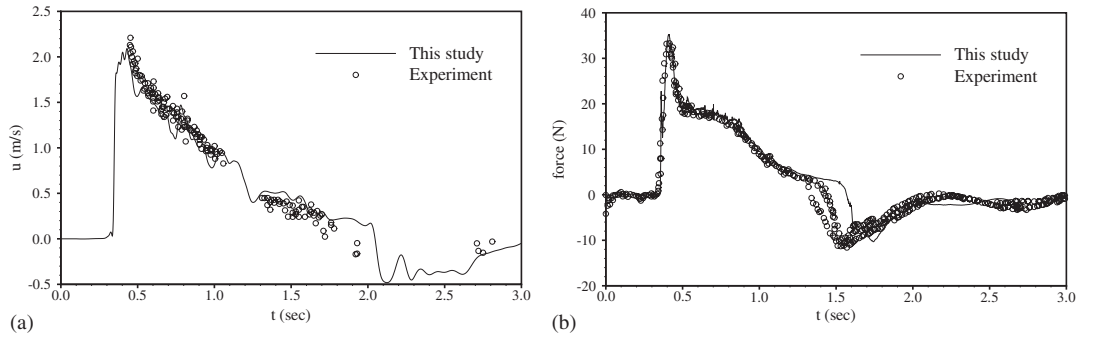

Figure 23. Comparison of numerical results with experimental data: (a) the x velocity component at a selected point in front of the column; and (b) the force acting on the column by collapsing water.

6. CONCLUSIONS

This paper presents a two-phase flow model that couples the incompressible Navier–Stokes solver with the level set method in the finite element framework to achieve maximum grid flexibility. Different from other methods, the current model is based on the fractional four-step method and the implicit characteristic Galerkin approximation without resorting to ENO schemes. The fractional four-step method is superior to other fractional step methods or SIMPLE-type algorithm because of easy implementation of the boundary condition for intermediate velocity. The accuracy of the Navier–Stokes solver is confirmed by the vortex decay test. The discretization schemes for the level set evolution and reinitialization equations are described. They are subsequently verified with the benchmark cases, including the reinitialization of a circle on two meshes, Zalesak's problem and the stretching of a circular fluid element in a swirling deformation velocity field.

The coupled system is finally applied to the benchmark cases of 2D solitary waves, and 2D and 3D broken dam problems without and with a square column. The computational results of these cases are in good agreement with the other existing experimental and numerical results.

ACKNOWLEDGEMENTS

C.-L. Lin and L. J. Weber acknowledge the financial support by ONR N00014-01-1-0262 and Public Utility District No. 2 of Grant County, Washington.

REFERENCES

1. Floryan JM, Rasmussen H. Numerical methods for viscous flows with moving boundaries. *Applied Mechanics Reviews* 1989; **42**:323–341.
2. Crowley WP. *Flag*: *A Free-Lagrangian Method for Numerically Simulating Hydrodynamic Flows in Two Dimensions*. Lecture Notes in Physics, vol. 8. Springer: Berlin, 1971; 37–43.
3. Hirt CW, Amsden AA, Cook JL. An arbitrary Lagrangian–Eulerian computing method for all speeds. *Journal of Computational Physics* 1974; **14**:227–253.

4. Güler I, Behr M, Tezduyar T. Parallel finite element computation of free-surface flows. *Computational Mechanics* 1999; **23**:117–123.
5. Sung J, Choi HG, Yoo JY. Time-accurate computation of unsteady free surface flows using an ALE-segregated equal-order FEM. *Computer Methods in Applied Mechanics and Engineering* 2000; **190**:1425–1440.
6. Harlow FH, Welch JE. Numerical study of large-amplitude free surface motions. *Physics of Fluids* 1965; **8**:2182–2189.
7. Hirt CW, Nichols BD. Volume of fluid (VOF) methods for the dynamics of free boundaries. *Journal of Computational Physics* 1981; **39**:201–225.
8. Kim MS, Lee WI. A new VOF-based numerical scheme for the simulation of fluid flow with free surface. Part I: new free surface-tracking algorithm and its verification. *International Journal for Numerical Methods in Fluids* 2003; **42**:765–790.
9. Osher S, Sethian JA. Fronts propagating with curvature-dependent speed: algorithms based on Hamilton–Jacobi formulations. *Journal of Computational Physics* 1988; **79**:12–49.
10. Osher S, Fedkiw RP. *Level Set Method and Dynamic Implicit Surfaces*. Springer: Berlin, 2002.
11. Sussman M, Smereka P, Osher S. A level set approach for computing solutions to incompressible two-phase flow. *Journal of Computational Physics* 1994; **114**:146–159.
12. Liu XD, Fedkiw RP, Kang M. A boundary condition capturing method for Poisson's equation on irregular domains. *Journal of Computational Physics* 2000; **160**:151–178.
13. Quecedo M, Pastor M. Application of the level set method to the finite element solution of two-phase flows. *International Journal for Numerical Methods in Engineering* 2001; **50**:645–663.
14. Zienkiewicz OC, Codina R. A general algorithm for compressible and incompressible flow: Part I. The split, characteristic-based scheme. *International Journal for Numerical Methods in Fluids* 1995; **20**:869–885.
15. Chessa J, Belytschko WP. An extended finite element method for two-phase fluids. *ASME Journal on Applied Mechanics* 2003; **70**:10–17.
16. Chorin AJ. A numerical solution of the Navier–Stokes equations. *Mathematics of Computation* 1968; **22**:745–762.
17. Brackbill JU, Kothe DB, Zemach C. A continuum method for modelling surface tension. *Journal of Computational Physics* 1992; **100**:335–354.
18. Unverdi SO, Tryggvason G. A front-tracking method for viscous, incompressible, multi-fluid flows. *Journal of Computational Physics* 1992; **100**:25–37.
19. Yue W, Lin C-L, Patel VC. Numerical simulation of unsteady multidimensional free surface motions by level set method. *International Journal for Numerical Methods in Fluids* 2003; **42**:853–884.
20. Peng D, Merriman B, Osher S, Zhao H, Kang M. A PDE-based fast local level set method. *Journal of Computational Physics* 1999; **155**:410–438.
21. Comini G, Manzan M, Nonino C. Analysis of finite element schemes for convection-type problems. *International Journal for Numerical Methods in Fluids* 1995; **20**:443.
22. Zienkiewicz OC, Taylor RL. The finite element method. *Fluid Dynamics*, vol. 3 (5th edn). 2002; 52–53.
23. Choi HG, Choi H, Yoo JY. A fractional four-step finite element formulation of the unsteady incompressible Navier–Stokes equations using SUPG and linear equal-order element methods. *Computer Methods in Applied Mechanics and Engineering* 1997; **143**:333–348.
24. Kim J, Moin P. Application of a fractional-step method to incompressible Navier–Stokes equations. *Journal of Computational Physics* 1985; **59**:308–323.
25. Tafti D. Comparison of some upwind-biased high-order formulations with a second-order central-difference scheme for time integration of the incompressible Navier–Stokes equations. *Computers and Fluids* 2003; **42**(7):647–665.
26. Zalesak ST. Fully multidimensional flux-corrected transport algorithms for fluids. *Journal of Computational Physics* 1979; **31**:335–362.
27. Rider WJ, Kothe DB. Reconstructing volume tracking. *Journal of Computational Physics* 1998; **141**:112–152.
28. Rudman M. Volume-tracking methods for interfacial flow calculations. *International Journal for Numerical Methods in Fluids* 1997; **24**:671–691.
29. Leveque RJ. High-resolution conservative algorithms for advection in incompressible flow. *SIAM Journal on Numerical Analysis* 1996; **33**:627–665.
30. Ramaswamy B. Numerical simulation of unsteady viscous free surface flow. *Journal of Computational Physics* 1994; **90**:396–430.
31. Thé JL, Raithby GD, Stubley GD. Surface-adaptive finite-volume method for solving free surface flows. *Numerical Heat Transfer*, *Part B* 1994; **26**:367–380.
32. Chan RK-C, Street RL, Strelkoff T. Computer study of finite amplitude water waves. *Technical Report 104*, Department of Civil Engineering, Stanford University, CA, 1969.
33. Martin JC, Moyce WJ. An experimental study of the collapse of liquid columns on a rigid horizontal plate. *Philosophical Transactions of the Royal Society of London Series A* 1952; **244**:312–324.
34. Kelecy FJ, Pletcher RH. The development of a free surface capturing approach for multidimensional free surface flows in closed containers. *Journal of Computational Physics* 1997; **138**:939–980.

35. Gómez-Gesteira M, Dalrymple RA. Using a three-dimensional smoothed particle hydrodynamics method for wave impact on a tall structure. *Journal of Waterway*, *Port*, *Coastal*, *and Ocean Engineering* 2004; **130**:63–69.
36. Árnason H. Interactions between an incident bore and a free-standing coastal structure. *Ph.D. Dissertation*, University of Washington, Seattle, WA, 2005, in preparation.

